Edinburgh Research Explorer

Design of cold-formed ferritic stainless steel RHS perforated beams

Design of Cold-formed Ferritic Stainless Steel RHS Perforated Beams

Zixuan Chen[a], Yuner Huang[b,*], Ben Young[c]

[a] *Institute of Architectural Engineering, Jiangsu Open University, Nanjing, Jiangsu, China (former address: School of Engineering, The University of Edinburgh, Edinburgh, Scotland, UK)*

[b] *School of Engineering, The University of Edinburgh, Edinburgh, Scotland, UK*

[c] *Department of Civil and Environmental Engineering, The Hong Kong Polytechnic University, Hong Kong, China*

ABSTRACT

Ferritic stainless steel has been increasingly used in construction industry due to its excellent mechanical properties and a relatively low price compared with other grades of stainless steel materials. Experimental and numerical investigation was performed to examine the structural behavior of ferritic stainless steel perforated beams. The experimental program consisted of twenty specimens of rectangular hollow sections subjected to four-point bending, based on which finite element model has been developed for further parametric study. The influence of hole size and section slenderness on the test and numerical specimens was evaluated. It was shown that moment capacity and curvature at ultimate moment had negligible effect for specimens with hole diameter up to 20% of web depth, but reduced when hole size beyond 20% of web depth in this study. The section slenderness of perforated beams was found to have little influence on reduction of moment capacity for the hole diameter up to 70% of web depth. The test and numerical results were also compared with design strengths predicted by the current direct strength method for cold-formed carbon steel perforated beams. It was shown that the current design rules provide conservative predictions to the cold-formed ferritic stainless steel perforated beams. In this study, modified design rules based on the direct strength method were proposed, and shown to improve the accuracy of these design rules in a reliable manner.

Keywords: Cold-formed steel; Direct strength method; Ferritic stainless steel; Finite element model; Perforated beam

* Corresponding author. Tel.: +44 (0) 131 650 5736; Fax: +44 (0) 131 650 6554.
  E-mail address: yuner.huang@ed.ac.uk

1 Introduction

Stainless steel has been increasingly used in various structural applications in recent years, in particular large structures in corrosive environment where long service life without maintenance is considered to be critical [1]. Among various stainless steel grades, ferritic stainless steel that features lower material cost, good ductility and impact resistance, is considered as a promising construction material [2]. Ferritic stainless steel has been used in constructions because of its aesthetic appearance, a high yield strength, ease of maintenance and a relatively low price compared with other type of stainless steel materials [2]. Cold-formed perforated beams are commonly used in constructions. With openings at web, electrical, plumbing and heating system can pass through the beams to beautify the ceilings as well as reduce the storey height of buildings, the self-weight of structural members and material cost. In the last decades, many researches on structural performance of cold-formed steel perforated beams had been carried out. The design recommendations for W-shaped beams with large web openings were given by Redwood and Shrivastava [3]. Chung et al. [4] conducted analytical and numerical investigation of the vierendeel mechanism in steel beams with circular web openings. Lian [5] studied the effect of holes on web crippling behaviour and found that the web crippling strength was mainly influenced by the ratio of the hole depth to the depth of the web and the ratio of the distance from the edge of the bearing to the flat depth of web. Besides, steel beams with novel shapes of web opening have been investigated, in order to serve aesthetic purpose and improve structural performance. Tsavdaridis and D'Mello [6,7] studied the primary structural characteristics for perforated steel sections with novel non-standard web opening shapes and proposed a simple design method for general practice. Durif et al. [8] investigated the failure modes of cellular beams with sinusoidal openings. Wang et al. [9] proposed fillet corner web openings on castellated steel beams to reduce the fabrication cost and improve the bearing capacity. Stainless steel has a fundamental different stress-strain behaviour from carbon steel. Thus, the design of cold-formed stainless steel perforated beam is an important issue. Yousefi et al. [10-13] studied the effect of web crippling on cold-formed duplex, ferritic and austenitic stainless steel lipped channel-sections. Fareed et al. [14]

conducted numerical investigations for the web crippling behaviour and the capacity of unlipped channel sections with non-circular web opening. Sonu and Singh [15] studied the shear behaviour of perforated lean duplex stainless steel rectangular hollow beams using finite element analyses.

The Direct Strength Method (DSM) is widely used to design members of complex cross-section because of its simplicity and reliability. In 1998, DSM was proposed by Schafer and Pekoz [16], and then was introduced in AISI specification in 2004 as an appendix to the specification. Moen [17] and Moen and Schafer [18] investigated the elastic buckling of cold-formed steel members with holes and then extended DSM to them. It shows that DSM is accessible and accurate to predict the strength of cold-formed steel perforated beams in global, local and distortional buckling limit state. The proposed DSM design equations for cold-formed steel members with holes have been specified in AISI S100-16 [19]. Considerable research has been conducted in recent years to develop the DSM for stainless steel structures. Lecce and Rasmussen [20, 21] proposed direct strength curves based on their distortional buckling tests on austenitic and ferritic stainless steel. Becque and Rasmussen [22-24] studied the local and overall buckling of austenitic and ferritic stainless steel, and showed that the current design method is conservative for lipped channel section, square and rectangular hollow section column.

However, there is still a research gap on the structural behaviour and design of ferritic stainless steel perforated beams. Therefore, the structural behaviour of cold-formed ferritic stainless steel rectangular hollow section perforated beams was investigated in this study. A series of four-point bending tests and an extensive parametric study were conducted. A total of 146 experimental and numerical results were compared with design strengths predicted by current direct strength method described in AISI S100-16 [19]. Reliability analysis was conducted, and a modified direct strength method design recommendation was proposed accordingly.

2 Experimental Investigation

Four point bending tests about major axis were conducted to obtain moment capacity of ferritic stainless steel perforated beams of rectangular hollow sections (RHS). A total of 18 specimens of cold-formed ferritic stainless steel with a circular hole at the web in the mid-span were tested. Bending tests of 4 specimens without holes were also conducted for comparison purpose. The relationship between bending moment and curvature of specimens was obtained. Therefore, the moment span (L_m) between the two loading points and the shear span (L_s) between the end supports and the loading points were carefully designed, so that the section moment capacity could be obtained without the occurrence of shear failure.

2.1 Test specimens

The test specimens were fabricated using cold-formed ferritic stainless steel of Grade EN 1.4003. The geometries of the beams are shown in Figure 1. The nominal specimen length (L) of all beams was equal to 1300 mm. The overall depth of web, width of flange, thickness of the cross-section, and diameter of the hole were represented by H, B, t and D, respectively. The outer radius and inner radius of corner regions of the cross-sections were r_o and r_i, respectively. The label $H{\times}B{\times}t$-D was used to represent different specimens with nominal geometries. There were four different sections and the nominal sizes of the section are 60×40×4, 80×60×4, 100×40×2 and 120×80×3. Each section had four different size of holes on the web and the nominal diameter of the holes (D) were equal to 0% (no hole), 20%, 50% and 80% of the flat portion of webs. Summary of the measured dimensions is shown in Table 1.

2.2 Test setup and procedure

2.2.1 Tensile coupon tests

Tensile coupon tests were conducted to determine the material properties of the cold-formed

ferritic stainless steel members. Longitudinal tensile coupons were extracted from both flat portion and corner of each section of the members. The material properties including the initial Young's modulus (E_0), static 0.2% proof stress ($f_{0.2}$), static ultimate tensile strength (f_u), strain at ultimate (ε_u), strain at fracture (ε_f), and Ramberg-Osgood parameter ($n = ln\ (0.01/0.2)/ln\ (f_{0.01}/f_{0.2})$) of the flat and corner portions were measured, where $f_{0.01}$ is the 0.01% proof stress, the subscripts "f" and "c" in the notations represent the material properties in the flat portion and corner portion of the sections, respectively.

The flat coupons were taken from the centre of the face at 90° from the weld for all member specimens. The dimensions of flat coupons conformed to the American Standard ASTM E 8M [25] for the tensile testing of metals. The gauge length of flat coupons was 50 mm with the width of 12.5 mm. The corner coupons had a gauge length of 25 mm with two holes at a distance of 20 mm from both ends. The diameter of the holes was 7 mm. The corner coupons were tested between two pins, so that the coupons were loaded through the centroid. An MTS testing machine was used in the coupon tests. Calibrated extensometers of 50 and 25 mm gauge lengths were mounted onto the flat and corner coupon specimens to measure the longitudinal strain during testing, respectively. Two linear strain gauges were attached at mid-length to the centre of both faces of each coupon. The testing procedure and loading rate recommended by Huang and Young [26] for ferritic stainless steel was adopted in the coupon tests.

2.2.2 Four-point bending tests

In order to simulate the pin-roller boundary condition, a half-rounded support and a roller support were placed at 45 mm from the two ends of test specimen. Vertical loading was applied through a lockable ball bearing connected to a spreader beam, and then the load transferred onto the two loading points of the specimen through rollers, as shown in Figure 2. The lockable ball bearing was used to eliminate any possible gaps between the spreader beam and the two loading points. The bearing was locked by four bolts and restrained from rotation before testing. The support and loading points were subjected to high shear force, and the loading points were also under high moment during

testing that may lead to pre-mature local buckling before bending failure occurs. Thus, web stiffening plates were clamped at four locations of each specimen. In addition, wooden blocks were inserted at the two loading points to prevent any possible local bearing failure during testing.

Three displacement transducers (LVDTs) were placed along the center line of the tension face of each specimen at the two loading points and the mid-span of the specimen. The vertical deflections of the specimen at these three locations were recorded, and the curvature of the specimen was calculated from the recorded deflections. Concentrated compressive force was applied by a hydraulic testing machine using displacement control with a constant loading rate of 1.0 mm/min for all test specimens. The static load was recorded by pausing the applied staining for 2 mins near the ultimate load. A data acquisition system was used to record the applied load and the readings of the LVDTs at regular intervals during the tests.

2.3 Test results

2.3.1 Material Properties

The stress-strain curves for flat and corner portions of the sections obtained from coupon tests are shown in Figures 3 (a) and (b), respectively. The static material properties obtained from the tensile coupon tests are summarized in Table 2. It is observed that the material properties at the corner regions are different from the flat regions, due to cold-forming effect. The 0.2% proof stress ($f_{0.2}$) at the corners are higher than those in the flat portions by 16% for section 60×40×4 and up to 41% for section 120×80×3. Compared with flat portions, the ultimate strength (f_u) of corner portions is increased by 17% for section 100×40×2 and up to 32% for section 120×80×3. Besides, the strain at ultimate (ε_u) and Ramberg-Osgood parameter (n) is considerably reduced for corner coupons.

2.3.2 Moment Capacity

The failure mode and moment-curvature curves of each test specimen were obtained from the tests. The failed specimens of all sections are shown in Figure 4. At the ultimate load, local buckling

(L) at compression flange was observed for all specimens, except for specimens 60×40×4-D0 and 80×60×4-D0. Therefore, the failure modes for all specimens were combination of local buckling and flexural bending (L+F), except for specimens 60×40×4-D0 and 80×60×4-D0 that failed by pure flexural bending (F), as shown in Table 3. The tests showed that for the stocky sections, such as 80×60×4 and 60×40×4, yield line mechanism was observed at the lower part of the beam under tensile load due to the early occurrence of flexural bending, as shown in Figure 4 (a) and (b). For the slender sections, such as 100×40×2 and 120×80×3, yield line mechanism was not observed due to the early occurrence of local buckling at the upper part of the beam under compressive load, as shown in Figure 4 (c) and (d).

The experimental ultimate moments (M_u) and the corresponding curvatures (κ_u) of the test specimens are summarized in Table 3. The ultimate moments were calculated from the following Eq. (1) :

$$M_u = \frac{F_u}{2} \times L_s \tag{1}$$

where F_u is the ultimate static load recoded from the hydraulic testing machine, L_s is the shear span of the specimens. There is no out-of-plane bending observed during the tests.

The curvatures (κ_u) of the test specimens were calculated from the following Eq. (2) :

$$\kappa_u = \frac{1}{r} \tag{2}$$

where r is the radius of the curved beam specimens between the two loading points. The radius of the curved beam was calculated from displacements measured from the three LVDTs. The curvature between the adjacent LVDTs was assumed as the same.

The moment-curvature curves of section 60×40×4 specimens are plotted in Figure 5. It can be concluded that the flexural capability of perforated beams reduces with the increasing diameter of holes. The flexural capacity (M_u) and the corresponding curvature (κ_u) of the specimens with holes are compared with the specimens without holes. The reductions in ultimate moment and corresponding curvature due to the perforations are summarized in Figure 6. It shows that the

diameter of hole has less impact on the ultimate moment than the corresponding curvatures. Generally, the influence of the hole size on the ultimate moment for all sections is similar, but the influence of the hole size on the curvatures at ultimate moment is more significant for stocky sections (60×40×4 and 80×60×4) than the slender sections (100×40×2 and 120×80×3).

Generally, a small hole with diameter of 20% of the flat portion of web had negligible influence on both ultimate moment and the corresponding curvatures for all sections. The ultimate moment (M_u) of specimens 60×40×4-D-20, 80×60×4-D20 and 100×40×2-D20 are reduced by 0.66%, 0.44% and 1.44%, respectively, while the 120×80×3-D20 is improved by 0.94%. The corresponding curvature (κ_u) of specimens 60×40×4-D20, 80×60×4-D20 and 120×80×3-D20 are reduced by 0.61%, 1.51% and 1.23%, respectively, while the 100×40×2-D20 is improved by 4.92%. Such results suggested that perforated beams with small holes of diameter up to 20% of flat portion of web depth had similar structural performance as those beams without perforation in this study. For the four sections, the hole with diameter equals to 50% of the flat portion of web has similar influence on the ultimate moment. With a hole diameter equals to 50% of the flat portion of web, the ultimate moments of sections 60×40×4, 80×60×4, 100×40×2 and 120×80×3 are reduced by 6.24%, 4.93%, 10.04% and 6.37%, respectively. The ultimate moments of specimens 60×40×4-D80, 80×60×4-D80, 100×40×2-D80 and 120×80×3-D80 are reduced by 17.92%, 15.27%, 26.08% and 17.92%, respectively.

In addition to moment capacity, influence of perforation on curvature at ultimate load was investigated for the test specimens, as excessive deflection is not desirable in practice. For stocky sections of 60×40×4 and 80×60×4, the effect of the hole with diameter lager or equals to 50% of the flat portion of web on the corresponding curvatures is greater than the slender sections of 100×40×2 and 120×80×3. With a hole diameter equals to 50% and 80%, the corresponding curvatures are reduced by 57.02% and 69.11% for section 60×40×4, respectively; reduced by 57.76% and 70.38% for section 80×60×4, respectively; reduced by 31.97% and 46.29% for section 100×40×2, respectively; reduced by 33.36% and 42.53% for section 120×80×3, respectively.

3 Numerical Investigation

The finite element (FE) software ABAQUS 6.13 [27] was used to develop a numerical model of cold-formed ferritic stainless steel rectangular hollow section perforated beams. The numerical model was verified against the experimental results. An extensive parameter study was conducted using the verified model to generate a data pool. The experimental and numerical data were used to improve the design rules for stainless steel perforated beams.

3.1 Numerical modeling

3.1.1 Material Properties

To produce an accurate numerical model, the measured material properties of flat and corner portions of the sections were taken according to the experimental results in Table 2. The poisson's radio was taken as 0.3. The measured stresses σ and strains ε material properties were converted into the corresponding true stress σ_{true} and true plastic strains $\varepsilon_{\text{true}}^{\text{pl}}$ respectively using the following Eq. (3) and Eq. (4):

$$\sigma_{\text{true}} = \sigma(1 + \varepsilon) \tag{3}$$

$$\varepsilon_{\text{true}}^{\text{pl}} = In(1 + \varepsilon) - \frac{\sigma_{\text{true}}}{E}$$

$$\tag{4}$$

The true stress-strain curves of flat and corner portions used in the finite element model are shown in Figure 7(a) and (b), respectively.

3.1.2 Mesh

The eight-noded doubly-curved shell element with reduced integration and five degrees of freedom (S8R5) was used in flat portions and the eight-noded doubly-curved shell element with reduced integration and six degrees of freedom (S8R) was used in the corner portions. The eight-noded element is suitable to model initial curved geometries and the element with five degrees of freedom employed in flat plate portions can increase computational efficiency. The load transferring

parts were meshed with the same mesh size with the plate portion using the three-dimensional solid element (C3D6).

A mesh sensitivity analysis was performed to find the balance between computational efficiency and accuracy of results. Specimens 100×40×2-D0 and 120×80×3-D80 were chosen to be modeled to illustrate the impact of global mesh size for plate portions varying from 4mm×4mm to 10mm×10mm. The mesh size for corner was 5mm×5mm. Figures 8 (a) and (b) show moment-curvature curves obtained from numerical models with different mesh size for the two specimens.

It is clear that the mesh size for plate portion did not influent the behaviour of beams before ultimate moment, but the moment capacity after buckling decreased with the decreasing mesh size. The computational time decreased with increasing mesh size, as shown in Figure 8 (c), and the different is small when the mesh size is larger than 7mm. Hence, global mesh size of 7mm×7mm was employed in the flat plate portions.

3.1.3 Imperfections

The influence of local imperfections on the moment capacity was also evaluated with the numerical model. The measured local imperfections for sections 60×40×4, 80×60×4, 100×40×2 and 120×80×3 are equal to 0.249 mm, 0.265 mm, 0.341 mm and 0.467 mm, respectively. A static RIKS step was set up with imperfections based on eigenvalues analysis. Specimens 60×40×4-D80, 80×60×4-D0, 100×40×2-D50 and 120×80×3-D20 were chosen to be modeled to illustrate the impact of imperfections on numerical results of both stocky and slender sections. Comparisons among the experimental results, the numerical results with and without imperfections are presented in Table 3. The difference in ultimate moment between the experimental result and numerical result without imperfection ranged from 0.3% to 7.7%, while the difference in ultimate moment between the experimental result and numerical result with imperfection ranged from 5.0% to 9.6%, as shown in Table 3. The average difference in ultimate moment between the numerical result without and with imperfection is 3.8%, which is small. In order to reduce the computational cost and improve the calculation efficiency, the imperfection of the beams was ignored in the parametric study. The final

numerical model of ferritic stainless steel rectangular hollow section perforated beam is shown in Figure 9.

3.1.4 Boundary conditions

In the experiments, the support condition of the specimens was simple support. The compressive loads at loading points were applied on rollers and then transferred onto 90-mm-wide load transferring plates to the specimen. Therefore, four halves of cylinders were used in the numerical model as load transferring part to simulate the rollers and load transferring plates in tests, as shown in Figure 9. Reference points located at the middle of the contact surface were used to couple the load transferring parts and the specimen. The interaction between the specimen and the load transferring part was surface-to-surface hard contact. The Young's modulus of the load transferring parts was 10 times of the specimen to simulate rigid material.

The load transferring parts at load points were restrained against all degrees of freedom except for displacement in the *y-* and *z*-axis as well as the rotation about the *x* axis. One of the load transferring parts at the support point was restrained against all degrees of freedom except for the rotation about *x* axis while the other one at the support point allow an extra displacement in *z* axis. The compressive load was applied by a static RIKS step with displacement control method. The nonlinear geometric parameter (*NLGEOM) was chosen to deal with the large displacement analysis.

3.2 Validation of numerical model

The numerical model was validated against the experimental results in two steps. In the first step, the overall deformation behaviour and failure modes were validated. The deformations of the corresponding FE models are shown in Figure 10.

Two failure modes, namely combination of local buckling and flexural bending (L+F) and pure flexural bending (F), were observed in the test specimens, as explained in Section 2.3.2 of this paper. Failure modes of the numerical specimens were observed at the ultimate moment, and it was found

11

that the failure modes predicted by the FE models are identical to those obtained from the tests, as shown in Table 4. It shows that the moment-curvature curves of numerical analysis are in good agreement with the experimental results. The discrepancy in initial stiffness may be attributed to deformation of support frame during the test, but in the elastic region, the numerical model shows exact agreement with theoretical EI slope. In the second step, the ultimate moment (M_u) and corresponding curvatures (κ_u) obtained from the numerical analyses were compared with those obtained from the experiments. The comparisons shown in Table 4 illustrate that the mean value of M_{Exp}/M_{FEA} radio is 1.05 with a standard deviation (S.D) of 0.02 and the mean value of $\kappa_{Exp,u}/\kappa_{FEA,u}$ radio is 0.83 with a standard deviation (S.D) of 0.17. It can be concluded that the developed numerical model was accurate enough to predict the ultimate moment capacity, and can be employed to increase the pool of structural performance data by means of parametric study.

3.3 Parametric study

An extensive parametric study was performed using the validated numerical models. The key parameters that exert most influence on the moment capacity of perforated beams were considered in the parametric studies, including the aspect ratio (H/B), section slenderness ratio ($d/(t\varepsilon)$) and the web hole size (D).

A total of 146 specimens, including 18 experimental results and 128 numerical results, were investigated. The web depths (H) of 380mm and 300mm were used in 112 and 16 numerical analyses, respectively. Four different aspect ratios (H/B) were investigated: 0.69, 1.0, 1.33, 2.5. For each aspect ratio of section, the values of section thickness were taken as 1.5 mm, 2 mm, 3 mm and 4 mm. For each section, there were seven different holes on the web and the nominal diameters of the holes (D) are equal to 0%, 20%, 50%, 60%, 70%, 80% and 90% of flat portion of webs. Besides, models of section 300×120mm with four different thickness (1.5mm, 2mm, 3mm and 4mm) and four different hole size (0%, 50%, 70% and 90%) were simulated to increase the data density. Thus, the specimens were labeled such that the cross-section dimension, bending axis and hole size could be identified, as

shown in Table 4. The dimension at the front represents the cross-section ($H \times B \times t$), where H is the depth of web, and B is the width of flange. All specimens are subjected to major axis bending, except for the specimens of section 380×570×1.5, 380×570×2, 380×570×3 and 380×570×4 are subjected to minor axis bending. The letter "D" represents the hole diameter with respect to the flat portion of web in percentage. For example, the label 300×120×4-D70 implies that the section has a nominal web depth of 300 mm, flange width of 120 mm, thickness of 4 mm, and a hole of diameter 70% of the flat portion of the web plate. The stress-strain curves of flat and corner portions in section 120×80×3 that obtained from the tensile coupon tests were adopted in the numerical modelling of parametric study. The ultimate moments of all specimens are shown in Table 5.

It is observed from the parametric study results that the ultimate moment (M_u) decreases as hole size increases. The average reduction of ultimate moment for beams with different hole sizes with respect to the ultimate moment of beams without hole is shown in Figure 11. The ultimate moment almost remains unchanged when the hole diameter is 20% of the flat portion of web. When the hole diameter increases to 50%, 60%, 70%, 80% and 90% of flat portion of web depth, the ultimate moment decreases by 5.1%, 6.5%, 9.2%, 14.9% and 22.0% with respect to the beams without hole.

Furthermore, the relationship between moment reduction of specimens due to perforation and slenderness (λ_l) is plotted in Figures 12 and 13, in order to investigate the influence of section geometry and hole size on bending capacity. The vertical axis is the ratio between ultimate moments of beams with perforation to those without perforation ($M_{u,p}/M_{u,D0}$) The slenderness factor λ_l equals to $(M_{ne}/M_{crl})^{0.5}$, where M_{ne} is nominal flexural strength calculated by direct strength method and M_{crl} is critical elastic moment, as explained in Section 4.1 of this paper. It is found that the moment reduction is generally not influenced by slenderness for perforated beams with hole diameter up to 70% of web depth. However, for beams with large hole diameters of 80% or 90% of web depth, the reduction of moment capacity is less significant for slender sections, as shown in Figures 12 and 13.

4 Evaluation of design rules

4.1 Current Direct Strength Method

The direct strength method (DSM) for cold-formed carbon steel perforated beams prescribed in the North American Specification for the Design of Cold-formed Steel Structural Members (AISI) [19] were used to determine the design strengths of the ferritic stainless steel perforated beams in this study. The nominal flexural strength (M_{DSM}) for beams shall be determined by the minimum of the nominal flexural strength for lateral-torsional buckling (M_{ne}), local buckling (M_{nl}) and distortional buckling (M_{nd}). The slenderness factor $\lambda_l = (M_{ne}/M_{crl})^{0.5}$. All specimens in this study were not failed by lateral-torsional buckling, and there is no distortional buckling for rectangular hollow sections. Thus, the DSM for carbon steel is shown in the Eq. (5). It should be noted that the AISI Specification is developed for carbon steel materials, and thus the design strength determined by Eq. (5) is represented as $M_{DSM,CS}$:

$$M_{DSM,CS} = \begin{cases} M_{ne} & \lambda_l \leq 0.776 \\ \left(\dfrac{1}{\lambda_l^{0.8}} - \dfrac{0.15}{\lambda_l^{1.6}}\right) M_{ne} & \lambda_l > 0.776 \end{cases}$$

(5)

Becque et al. [28] proposed the DSM for austenitic and ferritic stainless steel members without holes and sections in compression, as shown in the Eq. (6). The design strength determined by Eq. (6) is represented as $M_{DSM,SS}$:

$$M_{DSM,SS} = \begin{cases} M_{ne} & \lambda_l \leq 0.55 \\ \left(\dfrac{0.95}{\lambda_l} - \dfrac{0.22}{\lambda_l^2}\right) M_{ne} & \lambda_l > 0.55 \end{cases}$$

(6)

The nominal flexural strength for lateral-torsional buckling $M_{ne} = M_y = S_f f_y$, where S_f is elastic section modulus of full unreduced section relative to extreme compression fiber and f_y

is design yield stress; The member yield moment of net cross-section $M_{ynet} = S_{fnet}f_y$, where S_{fnet} is net section modulus referenced to the extreme fiber at first yield; M_{crl} is critical elastic local buckling moment including the influence of holes. The critical elastic buckling moment (M_{crl}) of the net cross-section was obtained from a rational elastic finite strip buckling analysis for perforated sections [18] with a 5 mm half-wave length interval. The software CUFSM was used to obtain M_{crl}.

These results are compared with the curves from the DSM for carbon steel (Eq. (5)) and the DSM for stainless steel (Eq. (6)). Figure 14 shows that the DSM curve proposed for carbon steels fits very well the results for specimens when $\lambda_l > 0.776$ but gives conservative results when $\lambda_l \leq 0.776$. It is also shown that the DSM for stainless steel proposed by Becque et al. [28] gives conservative prediction for evaluation of moment capacity of such beams.

4.2 Reliability analysis

A reliability analysis was carried out using the experimental and numerical results in order to evaluate the structural performance of ferritic stainless steel perforated beams. The reliability index (β_0) can be calculated by the following equation in Section 6.2 of the ASCE 8-02 Specification [29], as shown in Eq. (7):

$$\emptyset = 1.5(M_m F_m P_m)e^{-\beta_0\sqrt{V_m^2+V_F^2+C_P V_P^2+V_Q^2}} \tag{7}$$

The resistance factor (ϕ) of 0.9 for flexural members with stiffened or partially stiffened compression flanges subjected to bending is recommended. The statistical parameters for flexural members $M_m = 1.10$, $F_m = 1.00$, $V_m = 0.10$ and $V_F = 0.05$, $V_Q = 0.21$. The correction factor $C_p = (1+1/n)m/(m-2)$ as shown in AISI S100 Specification [19] is adopted, where n is the number of specimens and $m = n-1$. The mean value (P_m) and coefficient of variation (V_P) of test-to-predicted ratio of ultimate moment (M_u/M_{DSM}) were calculated, as shown in Table 6. The

slenderness range was divided into two ranges ($\lambda_l \leq 0.776$ and $\lambda_l > 0.776$), and the reliability index with a resistance factor (ϕ) of 0.9 was obtained for every range, as well as the whole range. A target reliability index (β_0) of 2.50 for cold-formed stainless steel members is recommended in this study.

The prediction for all 146 specimens from the current DSM for carbon steel is relatively accurate, with the overall reliability index of 2.57. For the 21 specimens with λ_l smaller than or equal to 0.776, the DSM for carbon steel provides relatively conservative prediction, with the reliability index of 3.21. On the other hand, the DSM for carbon steel provides a good prediction for the 125 specimens with λ_l greater than 0.776, with the reliability index of 2.60. The current DSM for stainless steel provides a very conservation prediction, with the overall reliability index of 3.31. The reliability index of the DSM for stainless steel for 14 specimens with λ_l smaller than or equal to 0.55 and the 132 specimens with λ_l greater than 0.55 is 3.63 and 3.28, respectively. Compared with the DSM for stainless steel, the DSM for carbon steel provides more accurate prediction. Therefore, in order to provide a more accurate prediction for ferritic stainless steel RHS beams, the current DSM for carbon steel with λ_l smaller than or equal to 0.776 should be modified.

4.3 Modified DSM

The nominal flexural strength (M_{DSM}) in the direct strength method as calculated by Eq. (5) shows that the nominal flexural strength is equal to a constant value of nominal flexural strength for lateral-torsional buckling ($M_{DSM} = M_{ne}$), when λ_l is smaller than or equal to 0.776 ($\lambda_l \leq 0.776$). In this study, based on a total number of 21 data with λ_l smaller than or equal to 0.776, it is shown that the flexural strengths generally decrease linearly as λ_l increases. Furthermore, the flexural strength predictions using the current direct strength method are generally conservative. Therefore, it is recommended to modify the current direct strength

equation Eq. (5) to Eq. (8). The M_{crl} values of specimens with hole diameter up to 20% of web depth can be obtained assuming full cross-section to simplify design procedure, because perforation had negligible influence on moment capacity of these specimens.

$$M_{DSM}^{\#} = \begin{cases} (1.5 - \frac{0.5}{0.776}\lambda_l)M_{ne} & \lambda_l \leq 0.776 \\ \left(\frac{1}{\lambda_l^{0.8}} - \frac{0.15}{\lambda_l^{1.6}}\right)M_{ne} & \lambda_l > 0.776 \end{cases} \tag{8}$$

The design strength calculated by the modified DSM are represented by $M^{\#}_{DSM}$. The mean values of $M_u/M^{\#}_{DSM}$ for all specimens is 1.07 with COV of 0.108 and the reliability index is 2.59, as shown in Table 5. It also can be found that the reliability index for 125 specimens with $\lambda_l > 0.776$ is 2.60 and for 21 specimens with $\lambda_l \leq 0.776$ is 2.56, are all above and approach to the target reliability index 2.5. The comparison of the experimental and numerical results with the design values calculated by the current DSM and the modified DSM is shown in Figure 14. It can be concluded that the modified DSM for the cold-formed ferritic stainless steel perforated beams can provide more accurate predictions compared to the current DSM.

5 Conclusions

This paper presented an experimental and numerical investigation on structural behaviour of cold-formed ferritic stainless steel rectangular hollow section perforated beams. Four-point bending tests were conducted for 18 beam specimens with and without perforation. Finite element model was developed and validated against the experimental results. A wide range of parametric study that covered different hole sizes and section slenderness was performed to evaluate the influence of key geometric parameters on moment capacity. It was found that perforation had negligible influence on moment capacity and the corresponding curvature for the hole diameter up to 20% of web depth. For perforated beams with hole diameter larger than 20% of web depth, moment capacity reduced with hole size. Furthermore, section slenderness

was found to have little influence on reduction of moment capacity for the hole diameter up to 70% of web depth. For perforated beams with holes beyond 70% of web depth, reduction of moment capacity due to perforation was found to be more significant for stocky sections than slender sections. The numerical and test results were compared with the design predictions calculated by the current direct strength method in the North American Specification (AISI) [19]. It was shown that the current direct strength method provided conservative prediction to the specimens investigated in this study. Besides, the flexural strengths generally decreased linearly with λ_l when $\lambda_l \leq 0.776$. A modified direct strength method was proposed in this study, to facilitate the design of cold-formed ferritic stainless steel rectangular hollow section perforated beams. The modified direct strength method was shown to provide a more accurate and reliable prediction, especially for stocky specimens with λ_l smaller than 0.776.

Acknowledgements

References

[1] Backhouse A., Baddoo, N. R. (2021), "Recent developments of stainless steels in structural applications" Proceeding, The 9th European Conference on Steel and Composite Structures, Sheffield, UK.

[2] Cashell K. A., Baddoo N. R. (2014), "Ferritic stainless steels in structural applications". T*hin-Walled Structures*, 83: 169-181.

[3] Redwood R.G. and Shrivastava S.C. (2001), "Design recommendations for steel beams with web holes", *Canadian Journal of Civil Engineering*, 7(4): 642-650.

[4] Chung K. F., Liu T. C. H., Ko A. C. H. (2001), "Investigation on Vierendeel mechanism in steel beams with circular web openings". *Journal of Constructional Steel Research*, 57(5): 467-490.

[5] Lian Y. (2016), "Web crippling behaviour of cold-formed steel and stainless steel channel sections with web openings", PhD thesis, Queen's University Belfast.

[6] Tsavdaridis K.D., D'Mello C. (2012), "Optimisation of novel elliptically-based web opening shapes of perforated steel", *Journal of Constructional Steel Research*, 76: 39-53.

[7] Tsavdaridis K.D., D'Mello C. (2012), "Vierendeel bending study of perforated steel beams with various novel shapes of web openings through non-linear finite element analyses", *Journal of Structural Engineering, ASCE*, 138(10): 1214-1230.

[8] Durif S., Bouchair A., Vassart O. (2013), "Experimental tests and numerical modeling of cellular beams with sinusoidal openings", *Journal of Constructional Steel Research*, 82: 72-87.

[9] Wang P., Ma Q., Wang X. (2014) , "Investigation of Vierendeel mechanism failure of castellated steel beams with fillet corner web openings", *Engineering Structures*, 74: 44-51.

[10] Yousefi A. M., Lim J. B. P., Uzzaman A., Lian Y., Clifton G. C., Young, B. (2016), "Web

crippling strength of cold-formed stainless steel lipped channel-sections with web openings subjected to interior-one-flange loading condition", *Steel & Composite Structures*, 21 (3), 629-659.

[11] Yousefi A. M , Lim J. B. P., Clifton G. C. (2017). "Cold-formed ferritic stainless steel unlipped channels with web openings subjected to web crippling under interior-two-flange loading condition – Part I: Tests and finite element model validation". *Thin-Walled Structures*, 116: 333-341.

[12] Yousefi A. M , Lim J. B. P., Clifton G. C. (2017). "Cold-formed ferritic stainless steel unlipped channels with web openings subjected to web crippling under interior-two-flange loading condition – Part II: Parametric study and design equations". *Thin-Walled Structures*, 116: 342-356.

[13] Yousefi A. M., Uzzaman A., Lim J. B. P., Clifton G. C., Young B. (2017). "Numerical investigation of web crippling strength in cold-formed stainless steel lipped channels with web openings subjected to interior-two-flange loading condition". *Steel & Composite Structures*, 23(3): 363-383.

[14] Fareed I., Somadasa W., Poologanathan K., Gunalan S., Beatini V., Sivabalan S. (2019). "Web Crippling Behaviour of Cold-formed Stainless Steel Beams with Non-Circular Web Opening". *Proceedings, 14ᵗʰ Nordic Steel Construction Conference*, Copenhagen, Denmark, 3(3-4): 937-942.

[15] Sonu J. K , Singh K. D. (2021). "Shear behavior of stiffened single perforated lean duplex stainless steel (LDSS) rectangular hollow beams". *Journal of Constructional Steel Research*, 176: 106377.

[16] Schafer B.W., Pekoz T. (1998). "Direct Strength Prediction of Cold-Formed Steel Members using Numerical Elastic Buckling Solutions". *Proceedings, 14th International Specialty Conference on Cold-Formed Steel Structures,* St. Louis, MO, USA.

[17] Moen C. D. (2008). "Direct strength design of cold-formed steel members with perforations". *Doctoral Dissertation*, Johns Hopkins University.

[18] Moen C.D., Schafer B.W. (2010). "Extending direct strength design to cold-formed steel beams with holes", *Proceedings, 20th International Specialty Conference on Cold-formed Steel Structures*, St. Louis, MO, USA.

[19] AISI S100-16, North American Specification for the Design of Cold-formed Steel Structural Members, Washington, D.C., *American Iron and Steel Institute*, 2016.

[20] Lecce M., Rasmussen K. J. R. (2006). "Distortional buckling of cold-formed stainless steel sections: Experimental investigation". *Journal of Structural Engineering, ASCE*, 132(4): 497 - 504.

[21] Lecce M,. Rasmussen K. J. R. (2006). "Distortional buckling of cold-formed stainless steel sections: Finite element modeling and design". *Journal of Structural Engineering, ASCE*, 132(4): 505 - 14.

[22] Becque J., Rasmussen K. J. R. (2006). "Experimental investigation of the interaction of local and overall buckling of cold-formed stainless steel columns". *Research Report R873*, School of Civil Engineering, University of Sydney.

[23] Becque J., Rasmussen K. J. R. (2007). "Experimental investigation of the interaction of local and overall buckling of stainless steel I-columns". *Research Report R886*, School of Civil Engineering, University of Sydney.

[24] Becque J., Rasmussen K. J. R. (2008). "Numerical investigation and design methods for stainless steel columns failing by the interaction of local and overall buckling". *Research Report R888*, School of Civil Engineering, University of Sydney.

[25] ASTM. Standard test methods for tension testing of metallic materials. E8/E8M-13a West Conshohocken, USA: *American Society for Testing and Materials*, 2013.

[26] Huang Y. and Young B. (2014), "The art of coupon tests", *Journal of constructional steel*

research, 96: 159-175.

[27] ABAQUS (2013). Analysis user's manual. Version 6.13.

[28] Becque J., Lecce M., Rasmussen K. J. R. (2008), "The direct strength method for stainless steel compression members", *Journal of constructional steel research*, 64(11): 1231-1238.

[29] ASCE. Specification for the Design of Cold-Formed Stainless Steel Structural Members. ASCE Standard SEI/ASCE 8-02, Reston, VA, *American Society of Civil Engineers*, 2002.
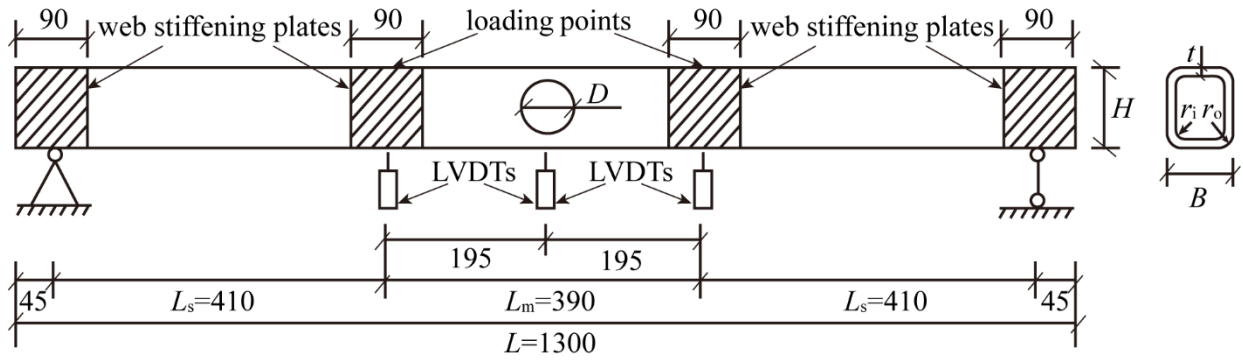
Figure 1: Geometries of the specimens (dimension in mm)
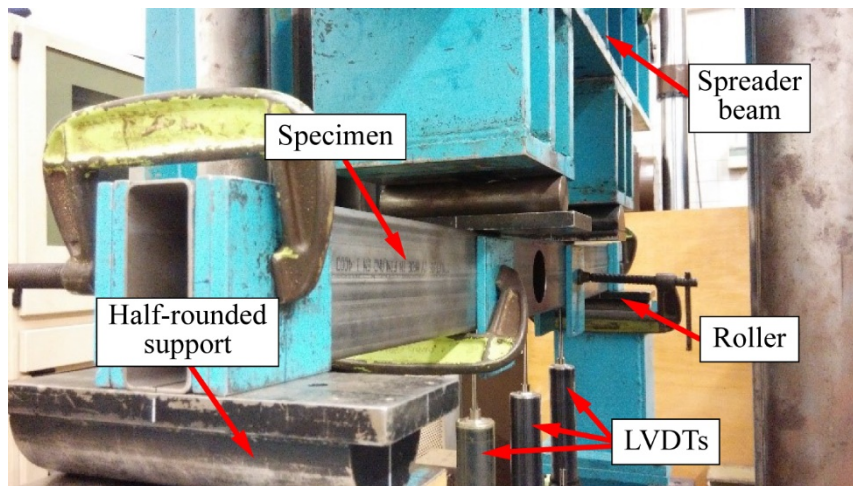
Figure 2: Setup of four-point bending tests
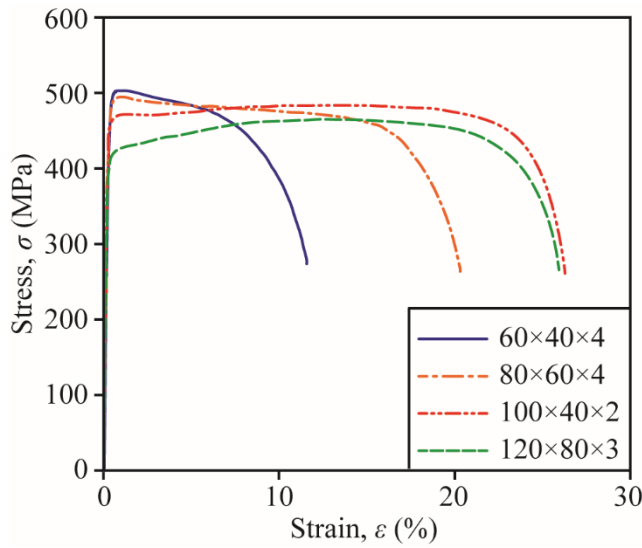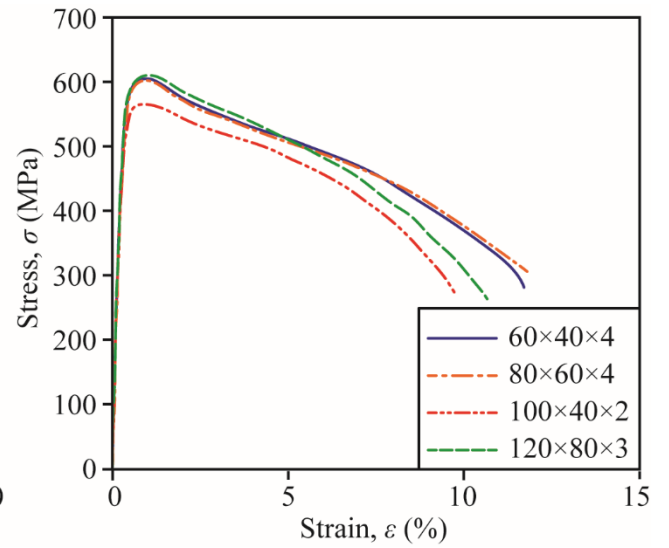
(a) Flat portions   (b) Corner portions

Figure 3: Stress-strain curves for different sections.

(a) Section60×40×4   (b) Section 80×60×4

(c) Section100×40×2   (d) Section 120×80×3
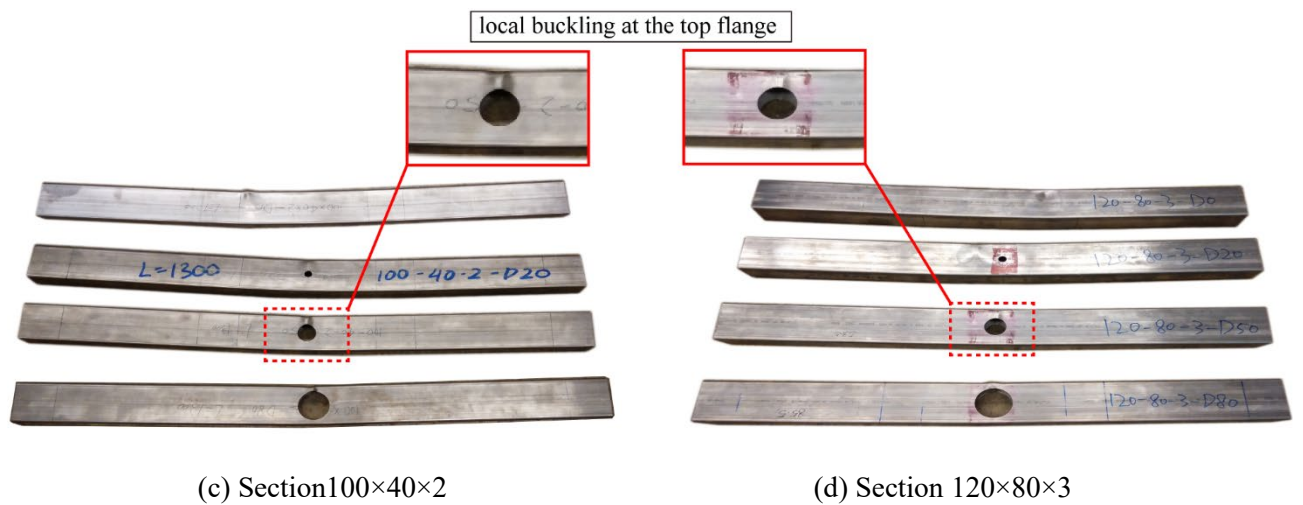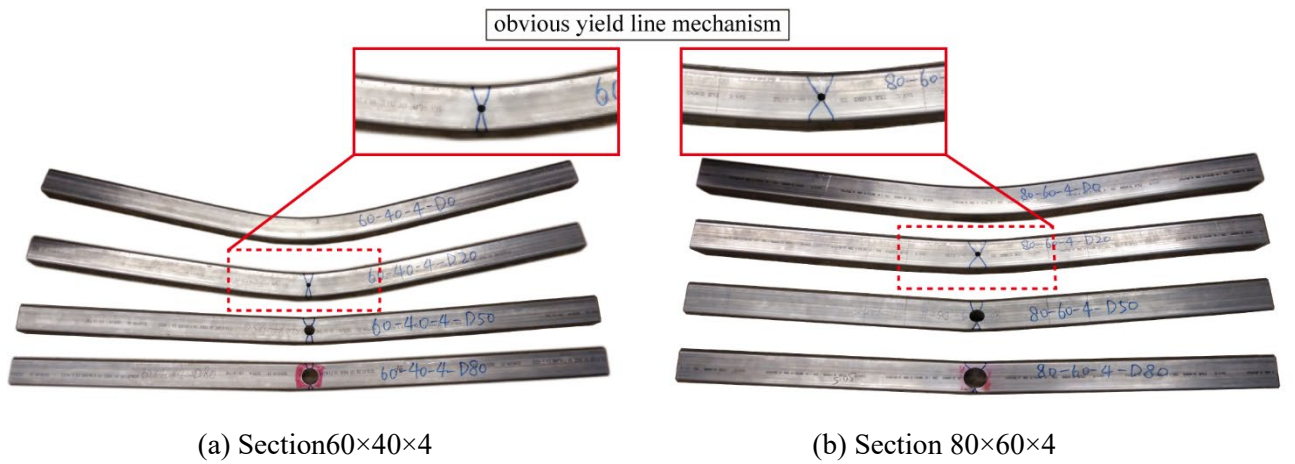
Figure 4: Failure modes of test specimens
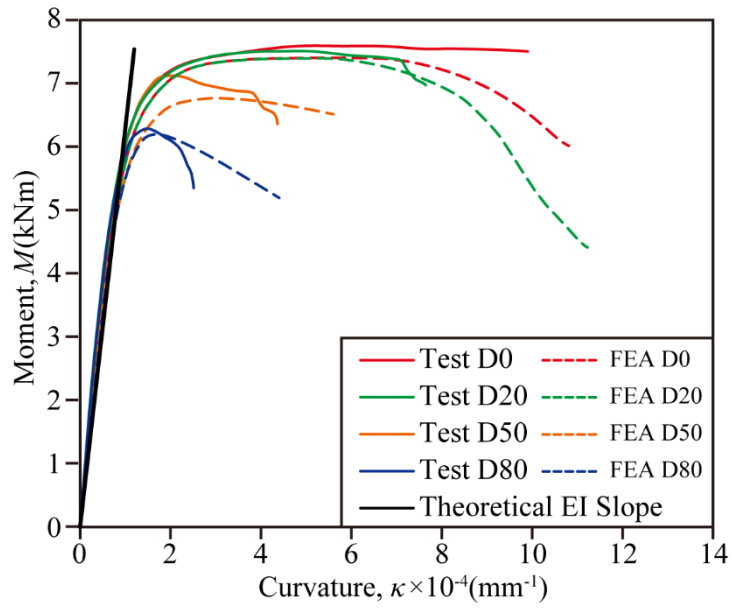
Figure 5: Moment-curvature curves of section 60×40×4 from tests and FE analyses
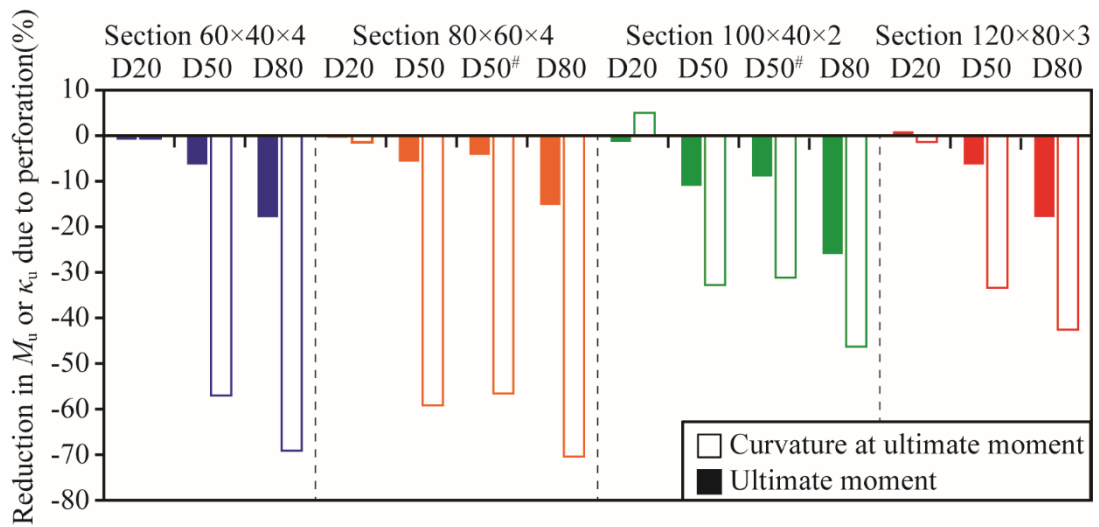
Figure 6: Influences of perforation on the ultimate moment and the corresponding curvature
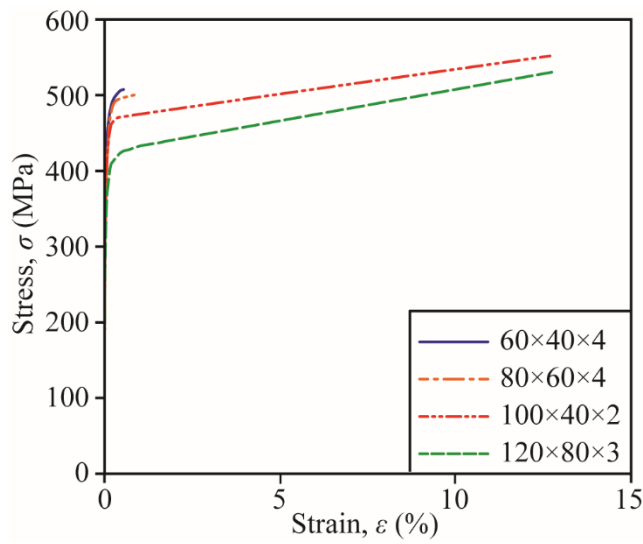
(a) Flat portions
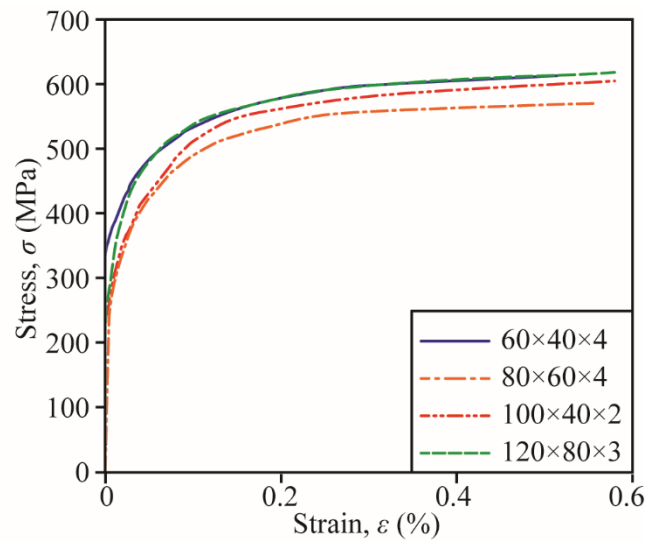
(b) Corner portions

Figure 7: True stress-strain curves used in FE model.
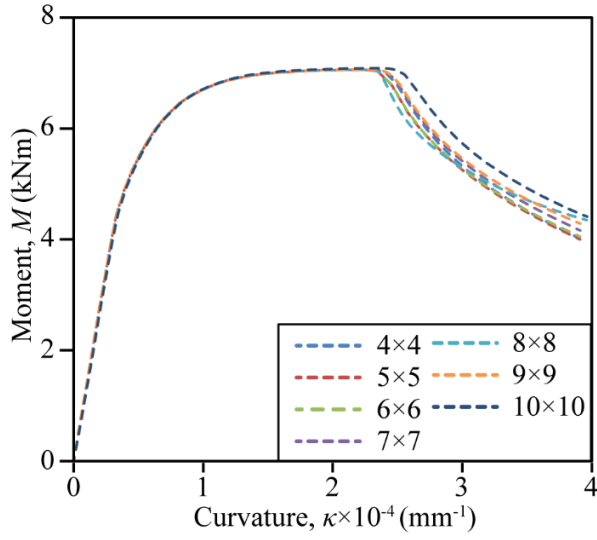
(a) Specimen 100×40×2-D0
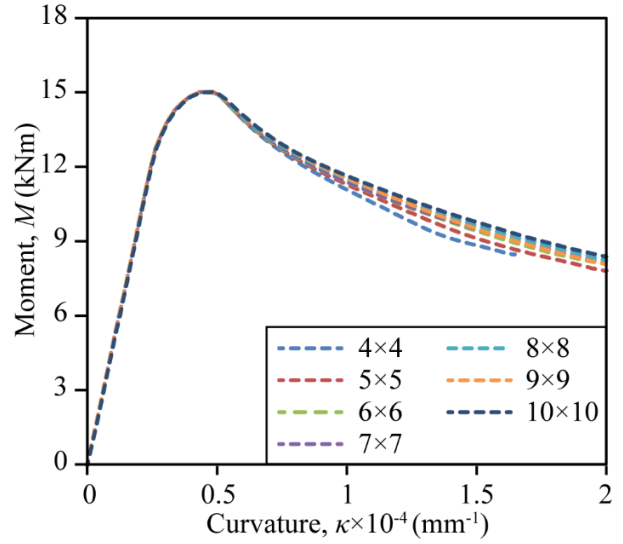
(b) Specimen 120×80×2-D80
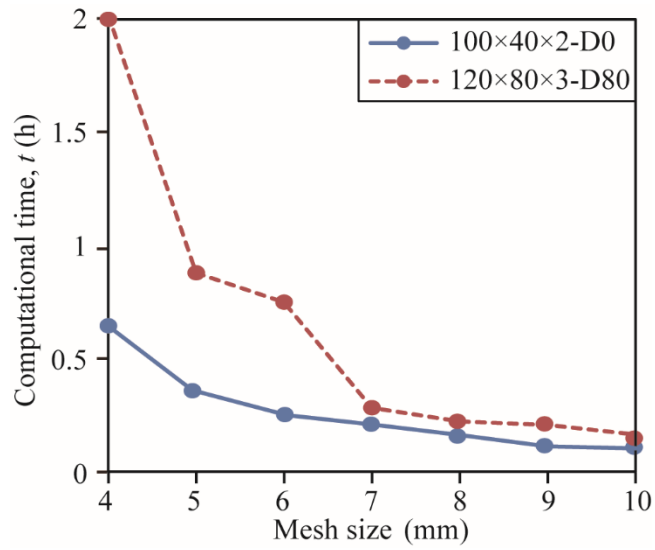
(c) Variation of computational time using different mesh size

Figure 8: Mesh sensitive analysis.
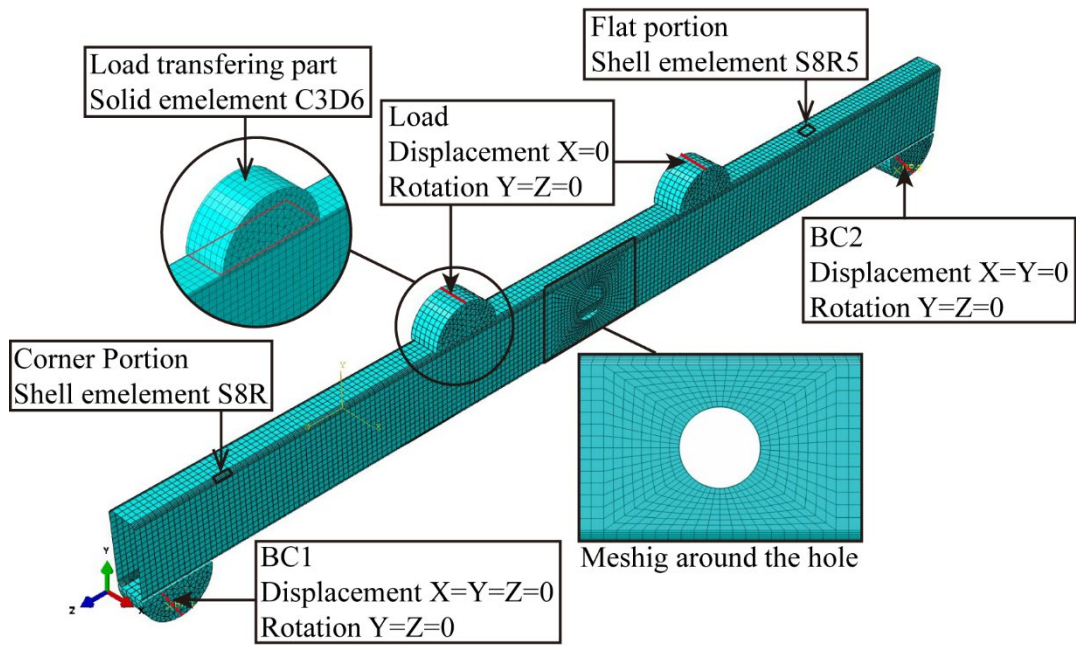
Figure 9: Numerical model of rectangular hollow section perforated beam

(a) Section 60×40×4

(b) Section 80×60×4

(c) Section 100×40×2

(d) Section 120×80×3
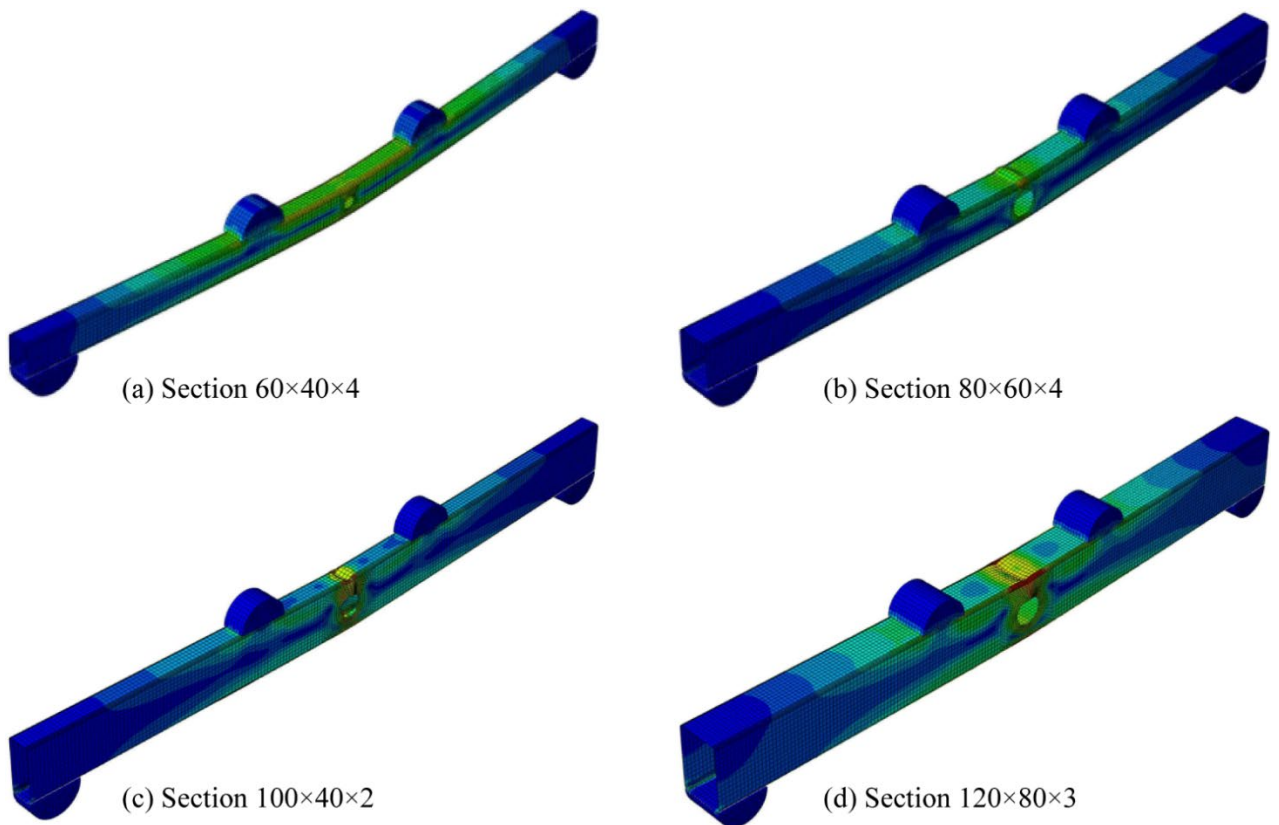
Figure 10: Failure modes of numerical model
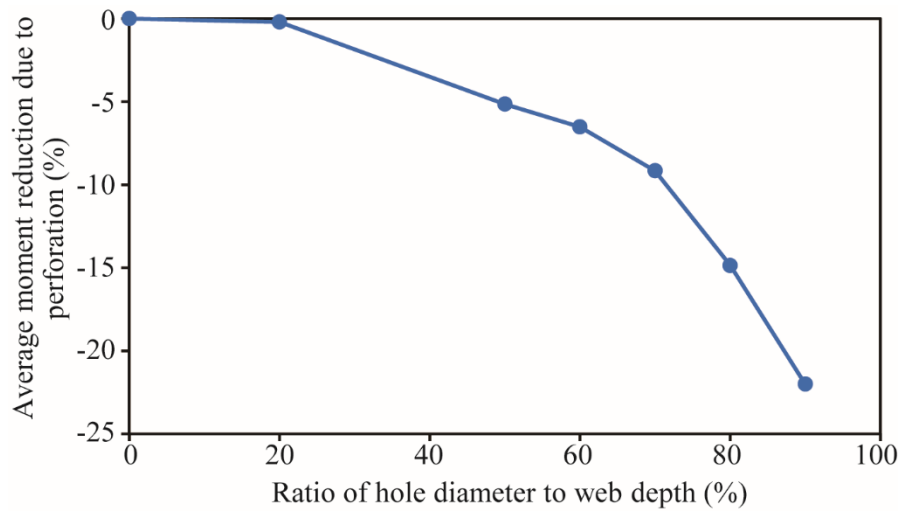
Figure 11: Average moment reduction due to different hole sizes
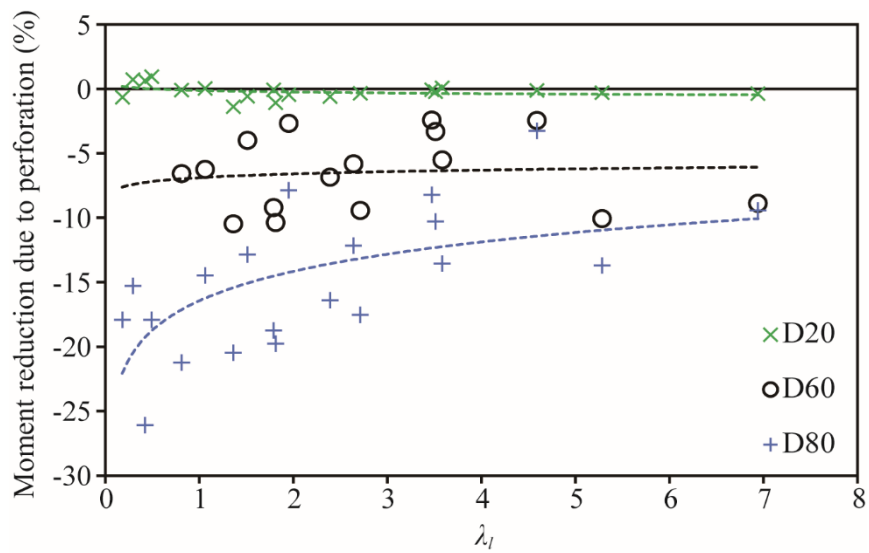
Figure 12: Moment reduction due to holes with diameter of 20%, 60% and 80% of web depth
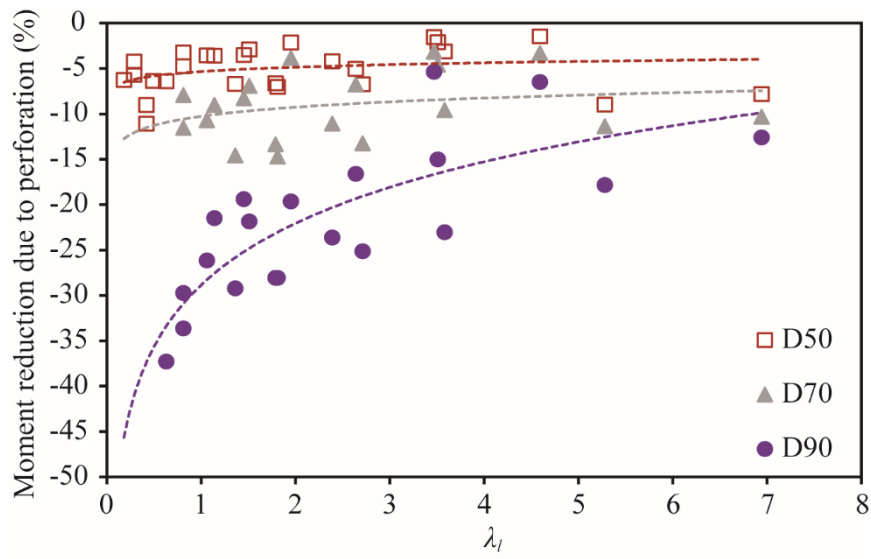
Figure 13: Moment reduction due to holes with diameter of 50%, 70% and 90% of web depth
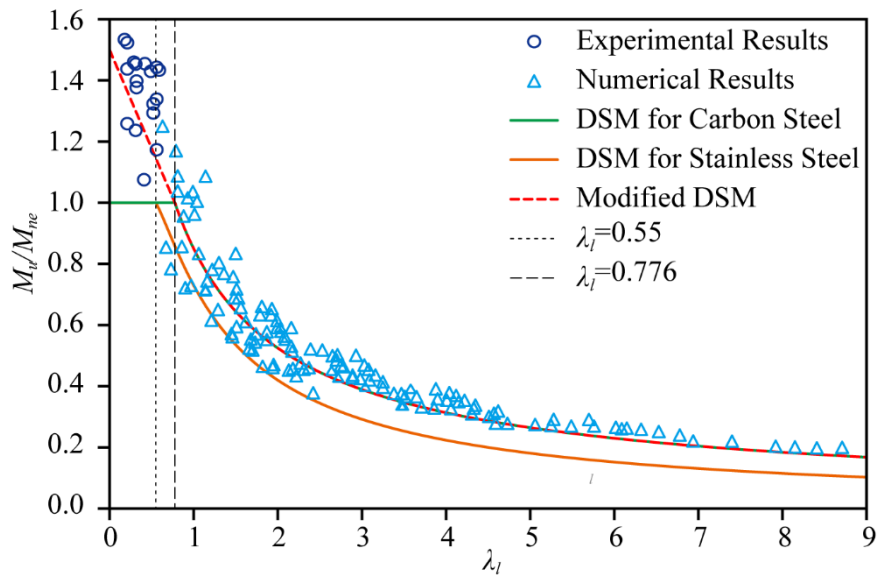
Figure 14. Comparison of experimental and numerical results with design strengths by different DSM

Table 1: Measured specimen dimensions

Specimen	L	H	B	t	r_o	r_i	D
			(mm)				(%)
60×40×4-D0	1301.0	60.07	40.24	3.87	7.63	4.44	0.00
60×40×4-D20	1290.0	60.08	40.44	3.96	7.63	4.44	20.30
60×40×4-D50	1300.5	59.88	40.21	3.90	7.63	4.44	50.78
60×40×4-D80	1301.0	60.05	40.17	3.79	7.63	4.44	80.12
80×60×4-D0	1301.5	80.35	60.31	3.74	8.38	4.94	0.00
80×60×4-D20	1299.0	80.51	60.15	3.79	8.38	4.94	19.54
80×60×4-D50	1299.6	80.32	60.13	3.77	8.38	4.94	49.58
80×60×4-D50[#]	1299.0	80.33	60.33	3.93	8.38	4.94	49.19
80×60×4-D80	1298.5	80.36	60.14	3.82	8.38	4.94	78.88
100×40×2-D0	1299.0	99.98	40.18	1.94	5.75	4.00	0.00
100×40×2-D20	1299.0	99.71	40.11	1.98	5.75	4.00	20.74
100×40×2-D50	1301.0	99.95	40.27	1.98	5.75	4.00	49.72
100×40×2-D50[#]	1299.0	100.06	40.54	1.95	5.75	4.00	49.52
100×40×2-D80	1299.0	100.03	40.31	1.99	5.75	4.00	79.96
120×80×3-D0	1301.0	120.02	80.3	2.89	6.63	4.13	0.00
120×80×3-D20	1299.5	120.25	80.4	2.88	6.63	4.13	20.12
120×80×3-D50	1301.0	120.47	79.97	2.84	6.63	4.13	49.82
120×80×3-D80	1305.0	120.55	80.37	2.89	6.63	4.13	79.73

[#] Repeated specimen

Table 2: Material properties obtained from tensile coupon tests

Section	flat						corner					
	$E_{0,f}$ (GPa)	$f_{0.2,f}$ (MPa)	$f_{u,f}$ (MPa)	$\varepsilon_{u,f}$ (%)	$\varepsilon_{f,f}$ (%)	n_f	$E_{0,c}$ (GPa)	$f_{0.2,c}$ (MPa)	$F_{u,c}$ (MPa)	$\varepsilon_{u,c}$ (%)	$\varepsilon_{f,c}$ (%)	$n_{,c}$
60×40×4	204.0	491.4	503.1	0.8	11.4	7.2	218.0	569.7	607.5	0.8	12.1	4.9
80×60×4	214.0	478.4	494.7	1.1	20.3	5.4	208.9	574.5	602.4	0.9	13.23	4.7
100×40×2	214.3	460.8	483.9	12.7	26.3	7.7	204.3	536.5	564.2	0.8	10.3	5.4
120×80×3	210.0	410.2	465.5	13.4	25.9	6.7	205.7	577.6	612.4	0.9	12.2	6.2

Table 3: Comparison of ultimate moments with and without local imperfections.

Specimen	Test $M_{Exp,u}$ (kNm)	FEA without imperfection $M_{FEA,u}$ (kNm)	FEA with imperfection $M_{FEA,imp,u}$ (kNm)	Difference bewteen $M_{Exp,u}$ /and $M_{FEA,u}$	Difference bewteen $M_{Exp,u}$ and $M_{FEA,imp,u}$	Difference bewteen $M_{FEA,u}$ and $M_{FEA,imp,u}$
60-40-4-D80	6.23	6.21	5.82	0.3%	6.6%	6.3%
80-60-4-D0	14.49	13.9	13.29	4.1%	8.3%	4.4%
100-40-2-D50	7.4	7.22	7.03	2.4%	5.0%	2.6%
120-80-3-D20	21.83	20.14	19.73	7.7%	9.6%	2.0%
Average				3.6%	7.4%	3.8%

Table 4: Experimental and numerical results

Specimen	Experimental results			Numerical results			Comparison	
	$\kappa_{Exp,u}\times 10^{-4}$ (mm^{-1})	$M_{Exp,u}$ (kNm)	Failure mode	$\kappa_{FEA,u}\times 10^{-4}$ (mm^{-1})	$M_{FEA,u}$ (kNm)	Failure mode	$\dfrac{\kappa_{Exp,u}}{\kappa_{FEA,u}}$	$\dfrac{M_{Exp,u}}{M_{FEA,u}}$
60×40×4-D0	4.92	7.59	F	5.13	7.41	F	0.96	1.02
60×40×4-D20	4.89	7.54	L+F	5.12	7.40	L+F	0.95	1.02
60×40×4-D50	2.11	7.12	L+F	3.00	6.76	L+F	0.70	1.05
60×40×4-D80	1.52	6.23	L+F	1.67	6.21	L+F	0.91	1.00
80×60×4-D0	3.23	14.49	F	3.10	13.90	F	1.04	1.04
80×60×4-D20	3.18	14.43	L+F	3.10	13.73	L+F	1.03	1.05
80×60×4-D50	1.32	13.67	L+F	1.58	13.38	L+F	0.83	1.02
80×60×4-D50$^{\#}$	1.41	13.88	L+F	1.58	13.38	L+F	0.89	1.04
80×60×4-D80	0.96	12.28	L+F	1.12	11.95	L+F	0.85	1.03
100×40×2-D0	1.22	8.32	L+F	2.35	7.83	L+F	0.52	1.06
100×40×2-D20	1.28	8.20	L+F	1.82	7.88	L+F	0.71	1.04
100×40×2-D50	0.82	7.40	L+F	0.94	7.22	L+F	0.87	1.02
100×40×2-D50$^{\#}$	0.84	7.57	L+F	0.94	7.22	L+F	0.89	1.05
100×40×2-D80	0.66	6.15	L+F	0.66	5.83	L+F	1.00	1.05
120×80×3-D0	0.81	21.63	L+F	1.21	20.16	L+F	0.67	1.07
120×80×3-D20	0.80	21.83	L+F	1.21	20.14	L+F	0.66	1.08
120×80×3-D50	0.54	20.26	L+F	1.13	19.05	L+F	0.48	1.06
120×80×3-D80	0.47	17.75	L+F	0.47	16.04	L+F	0.98	1.11
						Mean	0.83	1.05
						S.D.	0.17	0.02

Note: F = Flexural bending; L = Local buckling

Table 5: Comparison of experimental and numerical results with predicted results

Specimen	M_u (kNm)	$\dfrac{M_u}{M_{DSM,CS}}$	$\dfrac{M_u}{M_{DSM,SS}}$	$\dfrac{M_u}{M_{DSM}^{\#}}$	Specimen	M_u (kNm)	$\dfrac{M_u}{M_{DSM,CS}}$	$\dfrac{M_u}{M_{DSM,SS}}$	$\dfrac{M_u}{M_{DSM}^{\#}}$
60×40×4-D0	7.59	1.53	1.53	1.11	380×570×2-D90	51.05	1.15	1.78	1.15
60×40×4-D20	7.54	1.52	1.52	1.12	380×152×3-D0	103.53	1.02	1.19	1.02
60×40×4-D50	7.12	1.44	1.44	1.05	380×152×3-D20	103.57	1.29	1.56	1.29
60×40×4-D80	6.23	1.26	1.26	0.92	380×152×3-D50	99.86	1.13	1.34	1.13
80×60×4-D0	14.49	1.46	1.46	1.11	380×152×3-D60	97.06	1.05	1.24	1.05
80×60×4-D20	14.43	1.45	1.45	1.12	380×152×3-D70	92.44	0.97	1.14	0.97
80×60×4-D50	13.67	1.38	1.38	1.06	380×152×3-D80	88.54	0.92	1.07	0.92
80×60×4-D50$^{\#}$	13.88	1.40	1.40	1.08	380×152×3-D90	76.48	0.82	0.97	0.82
80×60×4-D80	12.28	1.24	1.24	0.95	380×286×3-D0	117.73	1.11	1.37	1.11
100×40×2-D0	8.32	1.45	1.45	1.18	380×286×3-D20	117.66	1.17	1.46	1.17
100×40×2-D20	8.20	1.43	1.47	1.28	380×286×3-D50	109.96	1.12	1.40	1.12
100×40×2-D50	7.40	1.29	1.29	1.11	380×286×3-D60	106.88	1.11	1.39	1.11
100×40×2-D50$^{\#}$	7.57	1.32	1.32	1.14	380×286×3-D70	102.02	1.08	1.35	1.08
100×40×2-D80	6.15	1.08	1.08	0.87	380×286×3-D80	95.65	1.04	1.32	1.04
120×80×3-D0	21.63	1.43	1.43	1.21	380×286×3-D90	84.70	0.96	1.23	0.96

120×80×3-D20	21.83	1.44	1.45	1.27	380×380×3-D0	119.52	1.13	1.45	1.13
120×80×3-D50	20.26	1.34	1.35	1.18	380×380×3-D20	118.81	1.17	1.52	1.17
120×80×3-D80	17.75	1.17	1.18	1.03	380×380×3-D50	114.51	1.17	1.53	1.17
380×152×1.5-D0	29.68	0.88	1.10	0.88	380×380×3-D60	111.33	1.15	1.51	1.15
380×152×1.5-D20	29.55	1.13	1.48	1.13	380×380×3-D70	106.29	1.13	1.48	1.13
380×152×1.5-D50	29.05	0.99	1.27	0.99	380×380×3-D80	99.94	1.09	1.44	1.09
380×152×1.5-D60	28.89	0.93	1.18	0.93	380×380×3-D90	91.30	1.03	1.38	1.03
380×152×1.5-D70	28.54	0.90	1.14	0.90	380×570×3-D0	123.92	1.15	1.58	1.15
380×152×1.5-D80	27.35	0.89	1.13	0.89	380×570×3-D20	124.01	1.22	1.70	1.22
380×152×1.5-D90	23.85	0.83	1.07	0.83	380×570×3-D50	120.08	1.22	1.71	1.22
380×286×1.5-D0	31.74	0.97	1.32	0.97	380×570×3-D60	117.09	1.21	1.70	1.21
380×286×1.5-D20	31.72	0.97	1.33	0.97	380×570×3-D70	112.04	1.18	1.66	1.18
380×286×1.5-D50	31.26	1.00	1.38	1.00	380×570×3-D80	107.12	1.15	1.64	1.15
380×286×1.5-D60	30.97	1.02	1.42	1.02	380×570×3-D90	95.40	1.05	1.51	1.05
380×286×1.5-D70	30.74	1.05	1.48	1.05	380×152×4-D0	178.23	1.12	1.30	1.12
380×286×1.5-D80	29.13	1.04	1.48	1.04	380×152×4-D20	178.08	1.40	1.64	1.40
380×286×1.5-D90	30.04	1.14	1.63	1.14	380×152×4-D50	169.82	1.21	1.41	1.21
380×380×1.5-D0	32.34	0.99	1.42	0.99	380×152×4-D60	166.5	1.14	1.32	1.14

380×380×1.5-D20	32.30	1.01	1.46	1.01	380×152×4-D70	157.66	1.14	1.33	1.14
380×380×1.5-D50	31.87	1.05	1.54	1.05	380×152×4-D80	140.41	0.91	1.06	0.91
380×380×1.5-D60	31.55	1.07	1.57	1.07	380×152×4-D90	118.31	0.79	0.92	0.79
380×380×1.5-D70	31.28	1.10	1.63	1.10	380×286×4-D0	188.88	1.11	1.33	1.11
380×380×1.5-D80	31.29	1.14	1.71	1.14	380×286×4-D20	186.28	1.16	1.39	1.16
380×380×1.5-D90	30.25	1.15	1.74	1.15	380×286×4-D50	176.25	1.12	1.35	1.12
380×570×1.5-D0	35.40	1.08	1.67	1.08	380×286×4-D60	169.09	1.08	1.31	1.08
380×570×1.5-D20	35.27	1.13	1.77	1.13	380×286×4-D70	161.35	1.05	1.27	1.05
380×570×1.5-D50	32.64	1.10	1.75	1.10	380×286×4-D80	150.24	1.00	1.22	1.00
380×570×1.5-D60	32.26	1.11	1.78	1.11	380×286×4-D90	133.69	0.93	1.14	0.93
380×570×1.5-D70	31.76	1.12	1.81	1.12	380×380×4-D0	200.33	1.17	1.44	1.17
380×570×1.5-D80	32.06	1.16	1.89	1.16	380×380×4-D20	198.19	1.21	1.51	1.21
380×570×1.5-D90	30.95	1.16	1.89	1.16	380×380×4-D50	186.30	1.17	1.46	1.17
380×152×2-D0	49.77	0.93	1.12	0.93	380×380×4-D60	179.55	1.14	1.43	1.14
380×152×2-D20	49.48	1.19	1.51	1.19	380×380×4-D70	170.87	1.11	1.39	1.11
380×152×2-D50	48.34	1.05	1.30	1.05	380×380×4-D80	160.73	1.07	1.35	1.07
380×152×2-D60	47.78	0.98	1.21	0.98	380×380×4-D90	144.16	0.99	1.27	0.99
380×152×2-D70	46.34	0.93	1.14	0.93	380×570×4-D0	210.77	1.20	1.57	1.20

380×152×2-D80	43.37	0.88	1.07	0.88	380×570×4-D20	210.02	1.27	1.68	1.27
380×152×2-D90	38.90	0.83	1.02	0.83	380×570×4-D50	196.62	1.21	1.62	1.21
380×286×2-D0	56.36	1.05	1.37	1.05	380×570×4-D60	190.91	1.19	1.60	1.19
380×286×2-D20	53.53	1.02	1.34	1.02	380×570×4-D70	182.9	1.17	1.57	1.17
380×286×2-D50	53.53	1.07	1.42	1.07	380×570×4-D80	173.81	1.13	1.53	1.13
380×286×2-D60	53.09	1.09	1.45	1.09	380×570×4-D90	157.81	1.06	1.44	1.06
380×286×2-D70	52.56	1.10	1.48	1.10	300×120×1.5-D0	22.23	0.87	1.04	0.87
380×286×2-D80	49.51	1.08	1.46	1.08	300×120×1.5-D50	21.45	1.00	1.24	1.00
380×286×2-D90	47.00	1.08	1.47	1.08	300×120×1.5-D70	20.39	0.88	1.07	0.88
380×380×2-D0	56.40	1.06	1.45	1.06	300×120×1.5-D90	17.92	0.86	1.07	0.86
380×380×2-D20	56.28	1.09	1.50	1.09	300×120×2-D0	36.83	0.92	1.08	0.92
380×380×2-D50	55.23	1.12	1.57	1.12	300×120×2-D50	35.51	1.06	1.27	1.06
380×380×2-D60	54.54	1.13	1.59	1.13	300×120×2-D70	33.51	0.91	1.08	0.91
380×380×2-D70	53.81	1.15	1.62	1.15	300×120×2-D90	28.92	0.86	1.03	0.86
380×380×2-D80	50.60	1.11	1.58	1.11	300×120×3-D0	79.32	1.07	1.24	1.07
380×380×2-D90	47.95	1.10	1.58	1.10	300×120×3-D50	76.77	1.21	1.42	1.21
380×570×2-D0	62.11	1.15	1.70	1.15	300×120×3-D70	73.05	1.04	1.20	1.04
380×570×2-D20	61.92	1.22	1.82	1.22	300×120×3-D90	55.76	0.84	0.98	0.84

380×570×2-D50	56.55	1.16	1.75	1.16	300×120×4-D0	125.93	1.25	1.31	1.14
380×570×2-D60	55.86	1.17	1.77	1.17	300×120×4-D50	117.86	1.18	1.38	1.18
380×570×2-D70	55.07	1.17	1.79	1.17	300×120×4-D70	86.10	0.85	0.92	0.80
380×570×2-D80	53.59	1.17	1.80	1.17	300×120×4-D90	78.99	0.78	0.88	0.76

Table 6: Reliability analysis results

	$\dfrac{M_u}{M_{DSM,CS}}$			$\dfrac{M_u}{M_{DSM,SS}}$			$\dfrac{M_u}{M_{DSM}^{\#}}$		
	$\lambda_l \leq 0.776$	$\lambda_l > 0.776$	All	$\lambda_l \leq 0.55$	$\lambda_l > 0.55$	All	$\lambda_l \leq 0.776$	$\lambda_l > 0.776$	All
# of data	21	125	146	14	132	146	21	125	146
Mean (P_m)	1.34	1.07	1.11	1.38	1.41	1.41	1.09	1.07	1.07
COV (V_p)	0.146	0.104	0.138	0.092	0.164	0.159	0.126	0.104	0.108
Reliability Index (β)	3.21	2.60	2.57	3.63	3.28	3.31	2.56	2.60	2.58

Note: resistance factor $\phi = 0.9$